Supplementary Information (SI) for Energy & Environmental Science.

Supporting Information

One ultrasonic measurement for non-invasive and whole-life-cycle thermal diagnosis of lithium-ion batteries

Authors:
Lingshi Zhang,[a] Zhongbao Wei,[a*] Chunxia Liu,[a] Hongwen He,[a] Kailong Liu,[b] Guangmin Zhou,[c] Yunhui Huang,[d] Zhichuan J. Xu[e]

Address:
[a] School of Mechanical Engineering, Beijing Institute of Technology, Beijing, China.
[b] School of Control Science and Engineering, Shandong University, Jinan, China.
[c] Tsinghua Shenzhen International Graduate School, Tsinghua University, Shenzhen, 518055, Guangdong, China
[d] State Key Laboratory of Material Processing and Die & Mould Technology, School of Materials Science and Engineering, Huazhong University of Science and Technology, Hubei, China
[e] School of Materials Science and Engineering, Nanyang Technological University, Singapore 639798, Singapore

*Corresponding author. Email: weizb@bit.edu.cn (Zhongbao Wei)

Content of the Supplementary information:

Supplementary Text

Note S1. Ultrasonic measurement.

Ultrasound is high-frequency mechanical vibration that travels through fluid and solid media. In ideal fluid, the shear modulus and shear stress are nonexistent, leaving just normal stress. The only longitudinal wave propagates in the consistent orientation as the displacement direction of a particle in the medium, and its speed is indicated as:

$$c_L = \sqrt{\frac{K}{\rho}} \qquad \text{* MERGEFORMAT (1)}$$

where K is the bulk modulus, ρ is the density, and c_L is the longitudinal wave speed.

Unlike the liquid, the solid can withstand shear stress, permitting waves to travel longitudinally and transversely. The transverse wave propagates perpendicular to the displacement direction of the particle in the medium. The wave speed in solids can be calculated as:

$$c_L = \sqrt{\frac{K + \frac{4}{3}G}{\rho}} \qquad \text{* MERGEFORMAT (2)}$$

$$c_s = \sqrt{\frac{G}{\rho}} \qquad \text{* MERGEFORMAT (3)}$$

where G and c_s represent the shear modulus and transverse wave speed, respectively.

Once a wave collides with the interface between medium 1 and medium 2 at a normal angle, it is split into two parts: a certain fraction of the energy is transmitted while the rest is reflected. The allocation of transmitted and reflected energy is governed by the relative acoustic impedance of the two mediums. The acoustic impedance of the medium is defined as:

$$Z = \rho c \qquad \text{* MERGEFORMAT (4)}$$

where c is the wave speed. The reflection coefficient (R) denotes the proportion of reflected sound pressure to incident sound pressure, given by:

$$R = \frac{Z_2 - Z_1}{Z_1 + Z_2} \qquad \text{* MERGEFORMAT (5)}$$

where Z_1 and Z_2 are the acoustic impedance of medium 1 and medium 2, respectively. The more significant the acoustic impedance mismatch between two mediums, the more energy is reflected into medium 1. The acoustic impedance of gas is around 0.0004 MRayl, while that of solid or liquid is approximately 1-50 MRayl[1]. Such a vast disparity indicates that nearly all the ultrasonic energy is reflected at the gas-solid or gas-liquid interface.

Note S2. Δ*TOFc* of pulsating current.

The current primarily impacts the lithium distribution in electrodes. In particular, the lithium diffusion within the graphite is given by the Fick's second law:

$$\frac{\partial C_j}{\partial t} = D_j \frac{\partial^2 C_j}{\partial x^2}$$ * MERGEFORMAT (6)

where C_j is the lithium concentration, D_j is the diffusion coefficient, and x is the distance from the graphite-SEI interface. The initial condition for solving Eq. 6 is:

$$C_j = C_j^* \quad x \geqslant 0, t \leqslant 0$$ * MERGEFORMAT (7)

where C_j^* is the initial concentration. Eq. 7 indicates that the lithium is distributed evenly within the graphite prior to applying current. The boundary condition for semi-infinite diffusion far from the graphite-SEI interface can be expressed as:

$$C_j = C_j^* \quad x = \infty, t > 0$$ * MERGEFORMAT (8)

The concentration gradient at the graphite-SEI interface is dictated by the current density, and its boundary condition is given by:

$$-D_j \left.\frac{\partial C_j}{\partial x}\right|_{x=0} = \frac{i}{n_j F} \quad t > 0,\ x = 0$$ * MERGEFORMAT (9)

where i is the current density, n_j is the number of electrons transferred per equivalent of reactant in the electrochemical reaction, and F is Faraday's constant. Using the Laplace transform, the solution to Eq. 10 for direct current can be represented as:

$$C_j = C_j^* - \frac{i}{n_j F \sqrt{D_j}}\left[2\sqrt{\frac{t}{\pi}}\exp\left(-\frac{x^2}{4D_j t}\right) - \frac{x}{\sqrt{D_j}} erfc\left(\frac{x}{\sqrt{4D_j t}}\right)\right]$$ *
MERGEFORMAT (10)

The lithium concentration is normalized as follows:

$$y = \frac{C_j - C_j^*}{C_j^*}$$ * MERGEFORMAT (11)

which can be further described as:

$$y = -\frac{i}{n_j F \sqrt{D} C_j^*}\left[2\sqrt{\frac{t}{\Pi}}\exp\left(-\frac{x^2}{4D_j t}\right) - \frac{x}{\sqrt{D_j}} erfc\left(\frac{x}{\sqrt{4D_j t}}\right)\right]$$ *
MERGEFORMAT (12)

The pulsating current comprises two square wave pulses with distinct current densities and durations. The boundary conditions at $x = 0$ are given by:

$$-D_j \left.\frac{\partial C_j}{\partial x}\right|_{x=0} = \frac{i_1(t)}{n_j F} \quad 0 < t \leqslant t_1$$ * MERGEFORMAT (13)

$$-D_j \left.\frac{\partial C_j}{\partial x}\right|_{x=0} = \frac{i_2(t)}{n_j F} \quad t_1 < t \leqslant t_2$$ * MERGEFORMAT (14)

The pulsating current is depicted by the superposition of two square wave pulses. One has a current density of i_1 and a duration of (t_1 + t_2), while the other has a current density of (i_2-i_1) and a duration of t_2. According to the "superposition principle", the lithium concentration distribution during 0-t_1 and t_1-t_2 can be calculated by[2]:

$$C_j(x,t) = C_j^*(1 + y(i_1, x, t)) \quad 0 \leqslant t < t_1$$ * MERGEFORMAT (15)

$$C_j(x,t) = C_j^*(1 + y(i_1, x, t) + y(i_2 - i_1, x, t - t_1)) \quad t_1 \leqslant t < t_2$$ *
MERGEFORMAT (16)

Note S3. Battery heat production.

The heat production of lithium-ion batteries is divided into reversible heat, polarization heat and side reaction heat according to the source. The reversible entropy change in the battery's electrochemical reaction generates the reversible heat. In contrast, polarization heat refers to the heat generated by the energy consumption caused by ohmic polarization, activation polarization and concentration polarization during the charge and discharge process. The by-reaction heat is the heat generated by the electrochemical side reactions such as the SEI decomposition of charge/discharge and the electrolyte-electrode material action. The reversible heat may be endothermic or exothermic depending on the electrochemical reaction and electrode material. For other sources of heat production, all are exothermic processes. Due to the complexity of the heat production mechanism inside the battery, Eq. 17 describing the heat production process has many forms. The local heat production equation derived from the electrochemical reaction is as follows:

$$\dot{Q} = a_s i_n (\phi_s - \phi_e - V_{oc}) + a_s i_n \left(T\frac{\partial U}{\partial T}\right) + \sigma^{eff}(\nabla\phi_s)^2 + \kappa^{eff}(\nabla\phi_e)^2 + \frac{2R_g T\kappa^{eff}}{F}(t_+^0 - 1)\left(1 + \frac{d\ln f_\pm}{d\ln c_e}\right)\nabla\ln c_e.\nabla\phi_e$$

* MERGEFORMAT (17)

where, a_s is the surface area per unit volume of electrode particles, unit m^{2}m^{-3}. i_n denotes the current density, with units of Am^{-2}; φ_s and φ_e represent the electric potentials of the solid and liquid phases, respectively, with units of V; V_{OC} denotes the open-circuit voltage, with units of V; $\sigma^{eff}$is the effective conductivity of the solid phase, with units of S.m^{-1}; κ^{eff}represents the effective ionic conductivity of the electrolyte phase, with units of S.m^{-1}; R_g is the universal gas constant, valued at 8.3145Jmol^{-1}K^{-1}; F denotes the Faraday constant, valued at 96485Cmol^{-1}; t_+^0 is the transference number of the electrolyte; $f_\pm$ is the activation coefficient of molecular motion; c_e refers to the concentration of ions in the electrolyte, with units of mol.m^{-3}. The first three terms on the right side of Eq. 17 correspond to polarization heat, reaction heat, and Joule heating from electron transport in the solid phase, respectively. In comparison, the final two terms describe the Ohmic losses due to resistance to ion transport in the electrolyte. Eq. 17 provides a more precise depiction of the heat generated within the battery, involving many electrochemical parameters and increasing computational complexity. Therefore, a simplified model for battery thermal production is derived, as expressed below:

$$\dot{Q} = I(V_{OC} - V) - I\left(T\frac{dU_{OC}}{dT}\right)$$

* MERGEFORMAT (18)

where I is the current of the battery, V is the terminal voltage, and dU_{OC}/dT is the entropic coefficient. In the first term on the right side of Eq. 18, $(V_{OC} - V)$ represents the overpotential of the battery, $I(V_{OC} - V)$ denotes the irreversible heat of the battery, and the second term represents the reversible entropic heat. Eq. 18 only applies in scenarios with no phase changes or mixed reactions, no concentration gradients in the electrolyte, and no variations in the open-circuit voltage. Eq. 18 can also be expressed in the following form:

$$\dot{Q} = R_i I^2 - IT\frac{\Delta S}{aF}$$

* MERGEFORMAT (19)

where R_i is the internal resistance of the battery, ΔS is the entropy change, and a is the number of electrons involved in the reaction. According to the experimental data, the internal resistance and entropy change of the cylindrical SONY-US18650G3 battery are shown in Eq. 20 and Eq. 21[3], which are affected by temperature and SOC.

$$R_i = \begin{cases} 2.258 \times 10^{-6} SOC^{-0.3952} & T = 20°C \\ 1.857 \times 10^{-6} SOC^{-0.2787} & T = 30°C \\ 1.659 \times 10^{-6} SOC^{-0.1692} & T = 40°C \end{cases}$$ * MERGEFORMAT (20)

$$\Delta S = \begin{cases} 99.88SOC - 76.67 & 0 \leqslant SOC \leqslant 0.77 \\ 30 & 0.77 < SOC \leqslant 0.87 \\ -20 & 0.87 < SOC \leqslant 1 \end{cases}$$ * MERGEFORMAT (21)

The above describes several of the most used heat generation equations and selects the appropriate equation according to the application scenario in actual use. To calculate the accurate heat production rate, many electrochemical parameters need to be known and Eq. 17 must be selected. For scenarios where the accuracy of heat production rate is not required, the Eq. 18 or Eq. 19 is applied to reduce the difficulty of solving.

Note S4. Lumped capacitance model.

The dimensionless criteria number, Biot number (*Bi*), can be used to evaluate whether the thermal system can be regarded as a lumped capacitance model. In general, the lumped capacitance model has a high accuracy for systems with $Bi < 0.1$[4]. Specifically, *Bi* is defined by:

$$Bi = \frac{hl}{\lambda} \qquad \text{* MERGEFORMAT (22)}$$

where *h*, *l* and λ are the convective heat transfer coefficient, characteristic length, and thermal conductivity coefficient, respectively. *l* is equal to half of the thickness of pouch cells. Furthermore, the convective heat transfer coefficient can be expressed as:

$$h = \frac{1}{AR_{out}} \qquad \text{* MERGEFORMAT (23)}$$

where *A* is the area of the thermal model. It is worth noting that the commercial LIB cells can generally fulfill $Bi < 0.1$, considering their typical material property and configuration.

Since the fixation of the transducer triggers localized heat exchange, an independent thermal model should be established for the battery area corresponding to the ultrasonic transducer rather than the whole battery. It is acceptable to assume that the battery generates heat uniformly since the excellent thermal conductivity in the plane direction will compensate for the temperature differences caused by uneven heat generation. In the pulsating current, the reversible entropy term is wiped out in a period. To eliminate the additional error caused by constant resistance, the heat generation rate is given by:

$$\dot{Q} = |V - V_{OCV}(SOC)| \times I \times \frac{\left(\frac{D}{2}\right)^2 \times \pi}{a \times b} \qquad \text{* MERGEFORMAT (24)}$$

where *V*, $V_{OCV}(SOC)$ and *I* denote respectively the terminal voltage, open circuit voltage and current. *D*, *a* and *b* are the diameter of the ultrasonic transducer, the width and length of the battery, respectively.

Supplemental Experimental Procedures

The battery cell integrated with the transducer is placed into an environmental simulation chamber to replicate the experimental temperature conditions. The transducer is connected to an ultrasonic flaw detector outside the incubator via probe wires. The ultrasonic flaw detector sends excitation signals to the transducer and receives ultrasonic signals carrying the structural information of the battery. The transmission of ultrasonic waveform data is facilitated by connecting the ultrasonic flaw detector to a computer through a USB interface. Remote command controls written in Python operate the ultrasonic flaw detector, transmitting data at a specified frequency and recording the corresponding time points. The data transmission interval can be adjusted based on specific experimental requirements, with a minimum interval of 2 seconds. Thermocouples are affixed to the battery surface to measure its temperature, and additional thermocouples are placed within the environmental simulation chamber to capture the ambient temperature. The positive and negative electrodes are connected to charging and voltage acquisition lines, further linked to the battery testing system. Following a control program, the battery testing system conducts charge/discharge operations on the battery while collecting voltage, current, and temperature data, subsequently outputting the data to an electronic spreadsheet.

Taking the specific heat capacity test experiment at 25°C as an example, Figure S2 shows the changes in current, voltage and heat production rate. The AC pulse of 3C makes the terminal voltage of the battery fluctuate periodically, and the range is 3.62-3.74V. To avoid the calculation error of heat production rate caused by fixed resistance at multiple ambient temperatures, Eq. 18 was selected for calculation.

Since the temperature rise of the experiment is less than 5°C, the open circuit voltage is approximately equal to the terminal voltage before the AC pulse heating, while the reversible entropy heat cancelling each other in the pulse current of one cycle. The specific equation for calculating the heat production rate is as follows:

$$\dot{Q} = (V_{oc} - V) \times I \times \frac{\left(\frac{17.5}{2}\right)^2 \times \pi}{169 \times 199} \qquad \text{* MERGEFORMAT (25)}$$

where 17.5 is the diameter of the transducer, 169 and 199 are the length and width of the electrode, respectively.

Since the TOF shift of this process is only affected by the average temperature of the battery, which is $\Delta TOF = \Delta TOF_{\mathrm{t}}$, the average temperature of the battery is estimated according to the mapping between ΔTOF_{t} and temperature, and the calculation equation is as follows:

$$T_e = T_a + \frac{\Delta TOF}{k} \qquad \text{* MERGEFORMAT (26)}$$

where k is the change rate of ΔTOF_{t} with temperature. According to section 4.3.2, the expression for k is as follows:

$$k = 2a_2 \cdot T + a_1 \qquad \text{* MERGEFORMAT (27)}$$

Among them, since the magnitude and temperature rise of the quadratic coefficient a_2 are small, the temperature in the Eq. 27 is approximately the ambient temperature.

With the "relaxation-after-heating" procedures, the impact of SOC and current can be eliminated to allow an accurate thermal calibration via ultrasound. In specific, ΔTOF_s can be ignored since the variation of SOC is limited to 0.25% during the AC heating. The ΔTOF_c during AC heating, primarily dominated by the lithium distribution, can be analyzed with both simulations and experiments. Figure S3A and S3B display the simulated lithium distribution during the first discharge half-cycle (0-3 s) and charge half-cycle (3-6 s). It is shown that the lithium oxidizes to lithium-ions at the graphite-SEI interface during the discharge half-cycle, resulting in a steady drop of the lithium concentration. A reverse trend occurs during the charging half-cycle. Moreover, the lithium concentration has been affected by the AC current, especially at the graphite-SEI interface. The simulations are further conducted for more full cycles (6 s, 12 s, 18 s, 24 s, and 30 s), and the distributions of lithium concentration are shown in Figure S3C. It is discovered that the lithium concentration remains consistent at the end of difference cycles. Considering the weak change of lithium distribution, the impact of ΔTOF_c during AC heating can be focused on only one cycle for simplicity.

Experiments are further performed to validate the ignorable effect of AC current to the TOF shift. Specifically, the battery is subjected to a period of pulsating current test at multiple ambient temperatures, with the influence of short-term current on the temperature being disregarded, i.e. $\Delta TOF = \Delta TOF_c$, as shown in Figure S3D. Results show that the TOF remains unchanged at all ambient temperatures, indicating that ΔTOF_c can be disregarded during the AC excitation which means $\Delta TOF = \Delta TOF_t$.

Using ARC to measure cells such as capacitance is a compelling validation of the ultrasonic method for estimating specific heat capacity. In the experiment of using ARC to measure the specific heat capacity of the battery, the experimental equipment involved includes ARC of Thermal Hazards Technology EV^+ and auxiliary tools such as electronic scale, electric heating sheet, constant voltage power supply, two electric couples and aluminum tape. Before measuring the specific heat capacity of the battery, the capacity calibration test is first carried out on the two new batteries and then charged at the rate of 1C CC to SOC=50%, which is recorded as battery I and battery II respectively. After the two batteries are ready, the ARC-specific heat capacity test is carried out according to the method recommended by the device manufacturer.

First, an electronic scale was used to measure the mass of the two battery cells, which were recorded as m_1 and m_2 (kg). As shown in Figure S4A, use aluminum tape (known specific heat capacity is C_{pAl}) to stick the electric heating plate to the surface of a battery cell and then stick the two battery cells together to form a test sample of battery I-electric heating plate-battery II. As shown in Figure S4B, use aluminum tape to stick a thermocouple at the geometric center of the two outer surfaces of the test sample to measure its surface temperature. The test sample with the thermocouple is suspended inside the ARC to prevent the test sample from directly contacting the inner wall of the ARC and causing heat conduction. After the experiment starts, the ARC is set to adiabatic mode, and the test sample is kept at 0°C for a period to achieve thermal equilibrium. Subsequently, the ARC is set to exothermic mode, in which the temperature of the inner wall of the ARC tracks the temperature of the battery surface to produce an approximate adiabatic condition. At the same time, the constant voltage power supply begins to act on the electric heating plate to heat the test sample. Once the battery surface temperature measured by the two thermocouples reaches 50°C, ARC stops tracking the battery temperature, and the constant voltage power supply stops heating the test sample but continues to record the temperature of the ARC top, sidewall, bottom and battery surface for 2 hours. Remove the aluminum tape attached to the battery surface and test its weight, which is recorded as m_3.

Figure S5 records the temperature of the top, sidewall, bottom and battery surface in the ARC measurement of specific heat capacity experiment, and the temperature of the battery surface is always slightly higher than the temperature of the ARC inner wall. In the test phase, the ARC inner wall temperature tracks the battery surface temperature to create an approximate adiabatic environment so that the heat generated by the electric heating sheet entirely acts on the internal energy of the experimental sample, and the energy conservation equation is as follows:

$$P = C_{pTOT} \frac{dT}{dt}$$ * MERGEFORMAT (28)

where P is the heating power of the electric heating sheet, equal to the product of the voltage and current of the constant voltage power supply, which is 21.4W. The temperature change rate with time (dT/dt) is calculated based on the temperature of the battery surface; C_{pTOT} is the specific heat capacity of the experimental sample, and its expression is as follows:

$$C_{pTOT} = m_3 C_{pAl} + (m_1 + m_2) C_p$$ * MERGEFORMAT (29)

where, m_1 is 0.603kg, m_2 is 0.6kg, m_3 is 1.79784×10^{-3}kg. Thus, the specific heat capacity of lithium-ion batteries at multiple temperatures has been solved, and the specific heat capacity value has a reference value to verify the accuracy of ultrasonic estimation of the specific heat capacity of batteries.

Type or paste text here. This should be additional explanatory text, such as: extended technical descriptions of results, full details of mathematical models, extended lists of acknowledgments, etc. It should not be additional discussion, analysis, interpretation, or critique.

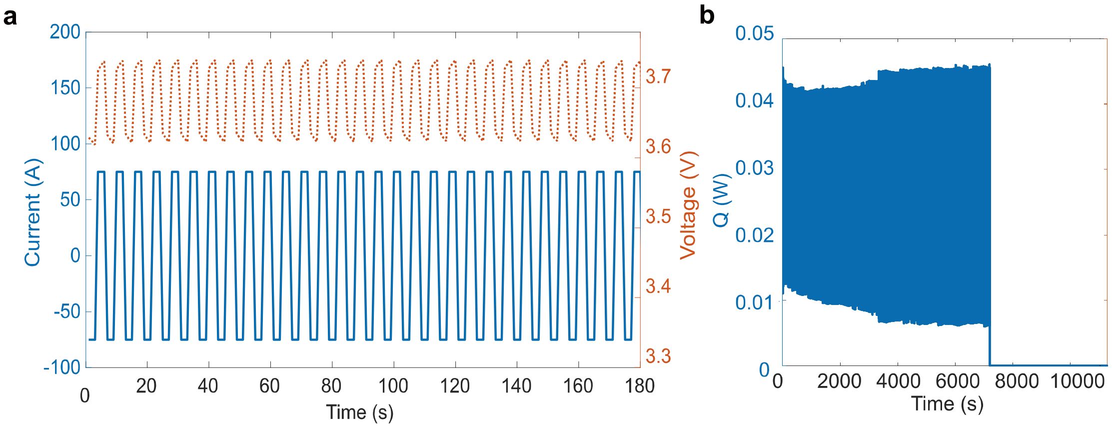

Fig. S1. AC pulse heating. (**a**) Current and voltage curve of AC pulse. (**b**) Heat production rate curve of AC pulse.

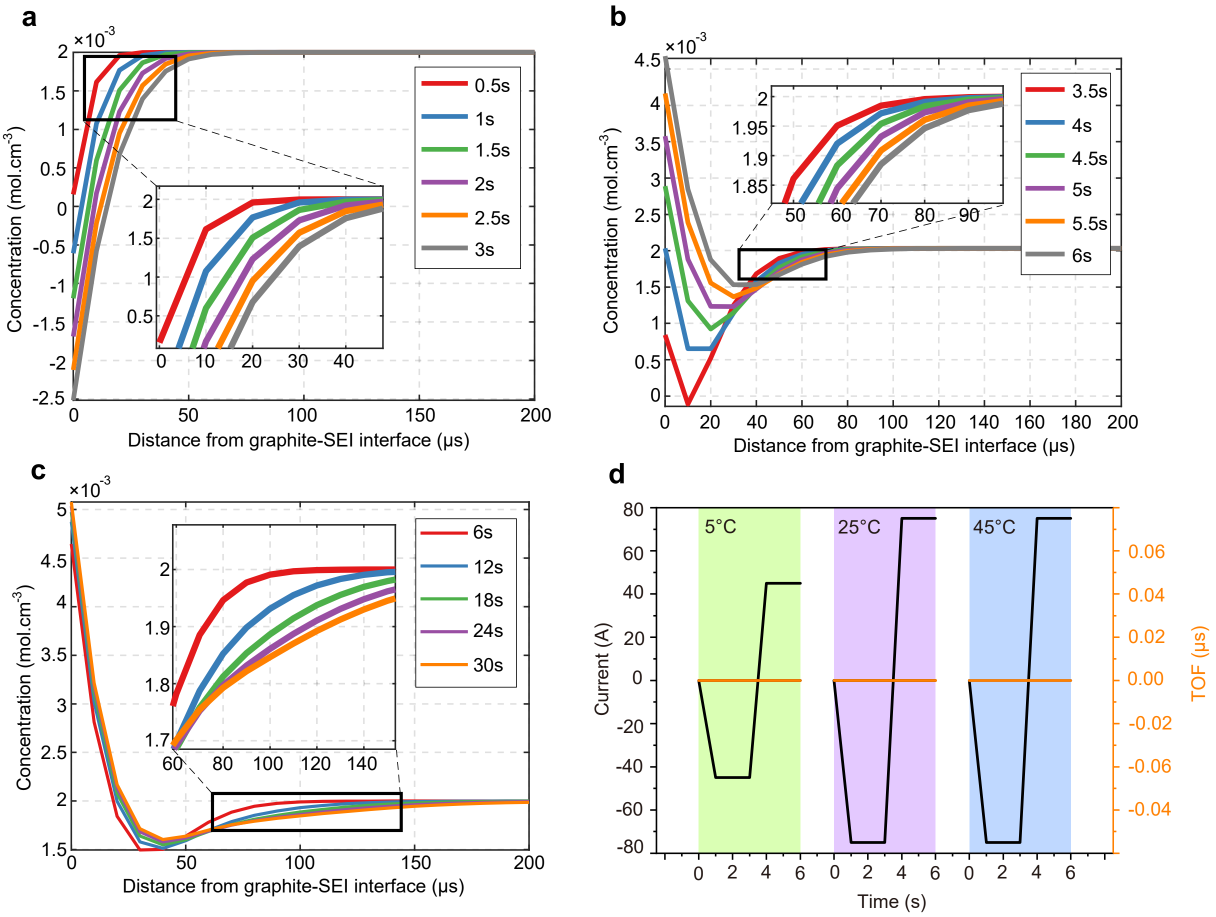

Fig. S2. Ignorable effect of AC current on the TOF shift. Simulated lithium distribution in graphite during (**a**) the first discharge half-cycle, (**b**) the first charge half-cycle, and (**c**) multiple full cycles. (**d**) Measured TOF shift in one period at different temperatures and load currents.

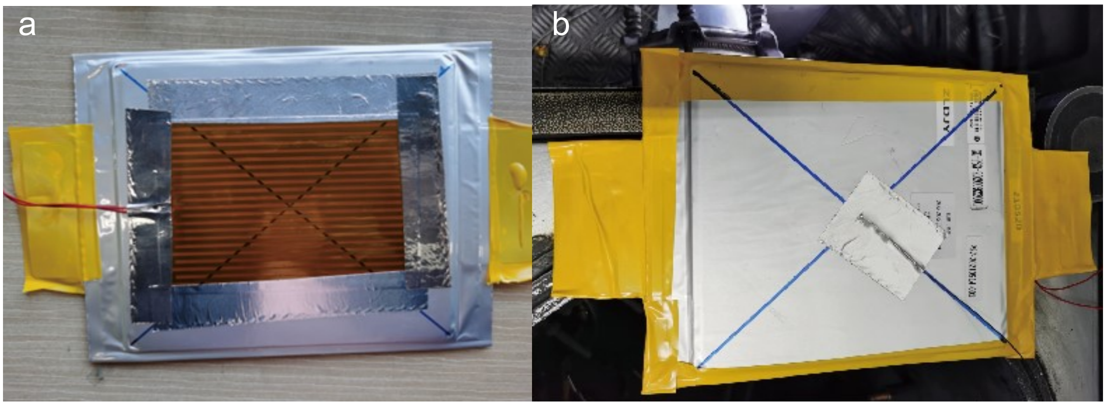

Fig. S3. ARC measurement of battery specific heat capacity of the actual diagram. (**a**) The electric heating plate paste position. (**b**) The thermocouple paste position.

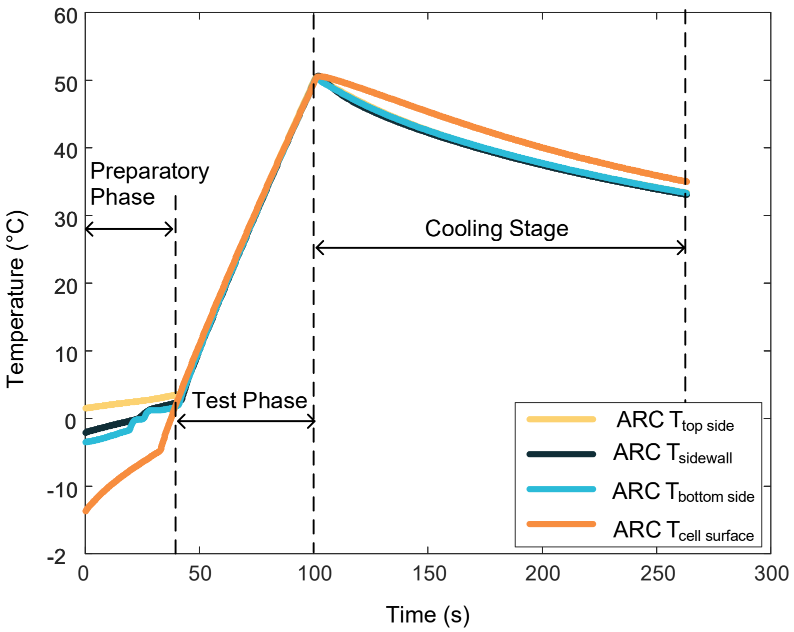

Fig. S4. The temperature results of ARC measuring specific heat capacity experiment.

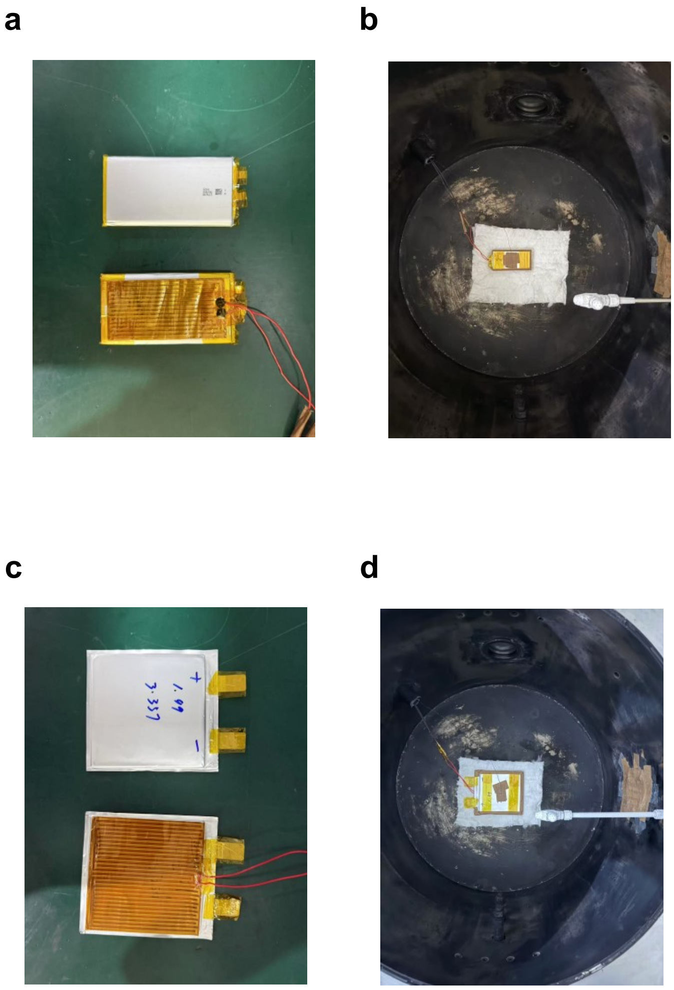

Fig. S5. ARC measurement of battery specific heat capacity of the NCM pouch cells and LFP pouch cells actual diagrams. The electric heating plate paste position of (**a**) NCM pouch cells and (**c**) LFP pouch cells. The ARC test setups for (**b**) NCM pouch cells and (**d**) LFP pouch cells.

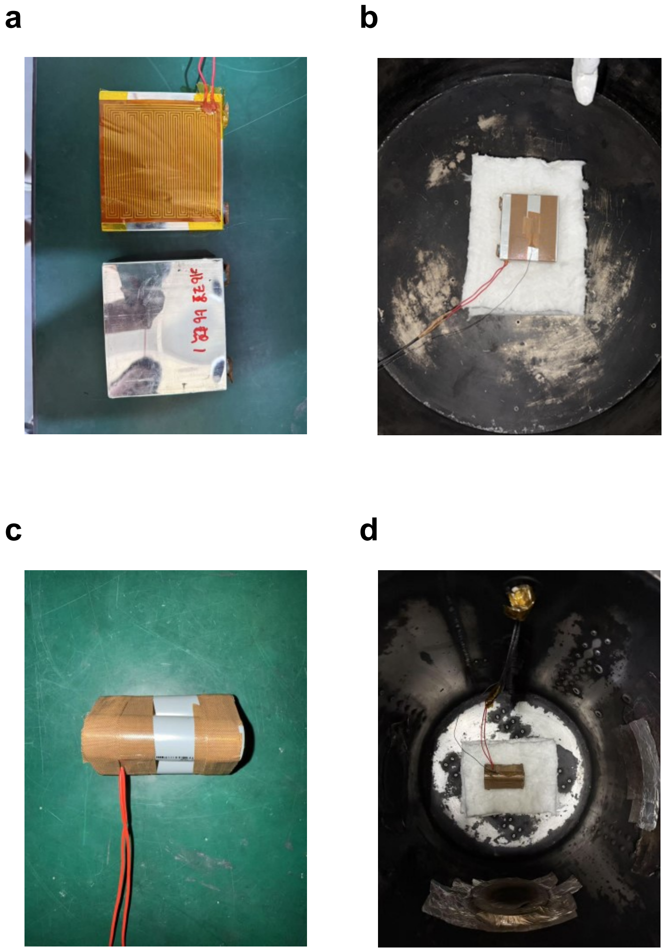

Fig. S6. ARC measurement of battery specific heat capacity of the LMO prismatic cells and NCM cylindrical cells actual diagrams. The electric heating plate paste position of (**a**) LMO prismatic cells and (**c**) NCM cylindrical cells. The ARC test setups for (**b**) LMO prismatic cells and (**d**) NCM cylindrical cells**.**

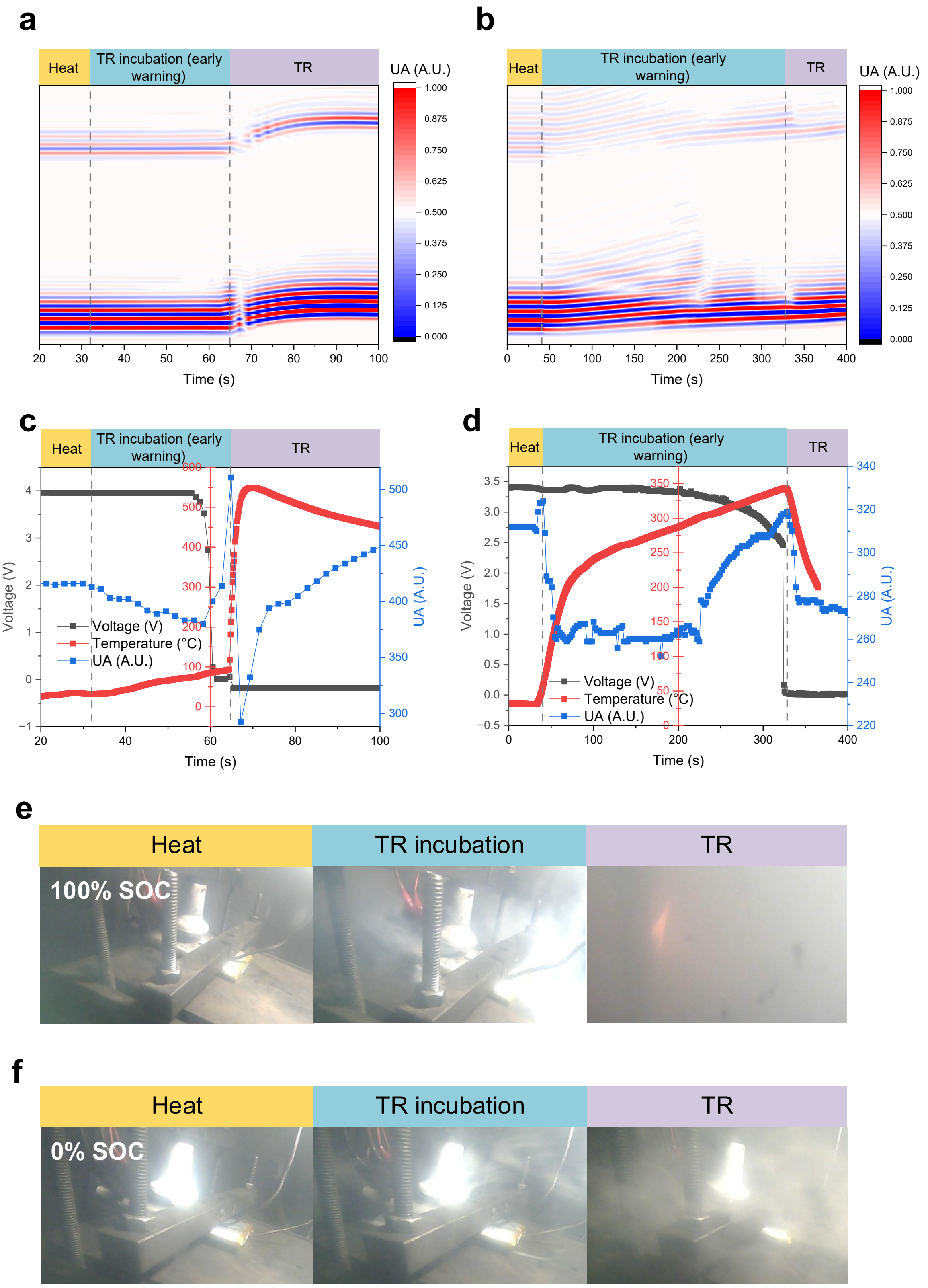

Fig. S7. Ultrasonic early warning of TR for NCM pouch cells. Heatmaps of ultrasonic waves for (**a**) 100% SOC and (**b**) 0% SOC cells. The change of UA, temperature and voltage during the TR of (**c**) 100% SOC and (**d**) 0% SOC cells. Photographs of thermal abuse process of (**e**) 100% SOC and (**f**) 0% SOC NCM pouch cells.

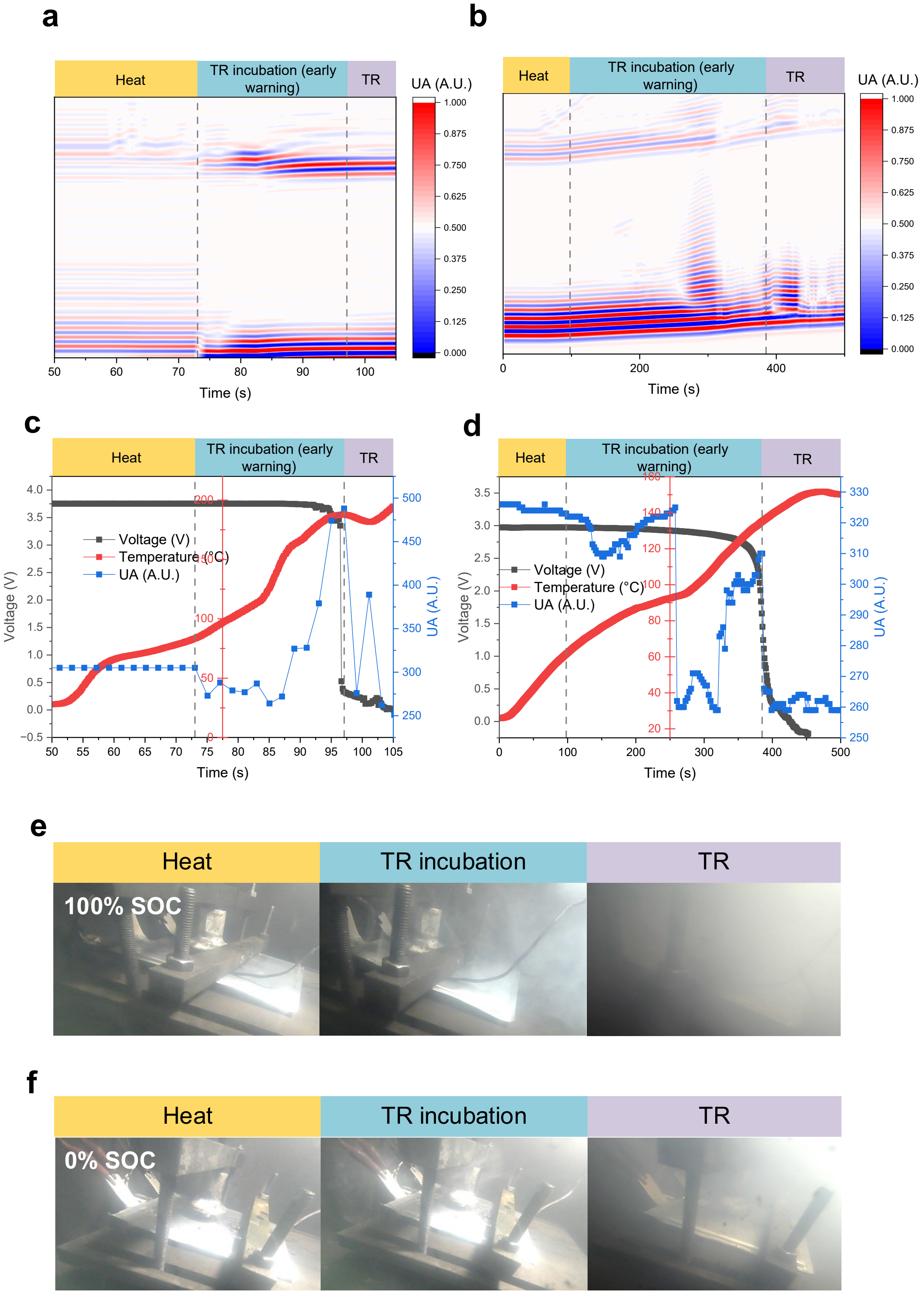

Fig. S8. Ultrasonic early warning of TR for LFP pouch cells. Heatmaps of ultrasonic waves for (**a**) 100% SOC and (**b**) 0% SOC cells. The change of UA, temperature and voltage during the TR of (**c**) 100% SOC and (**d**) 0% SOC cells. Photographs of thermal abuse process of (**e**) 100% SOC and (**f**) 0% SOC LFP pouch cells.

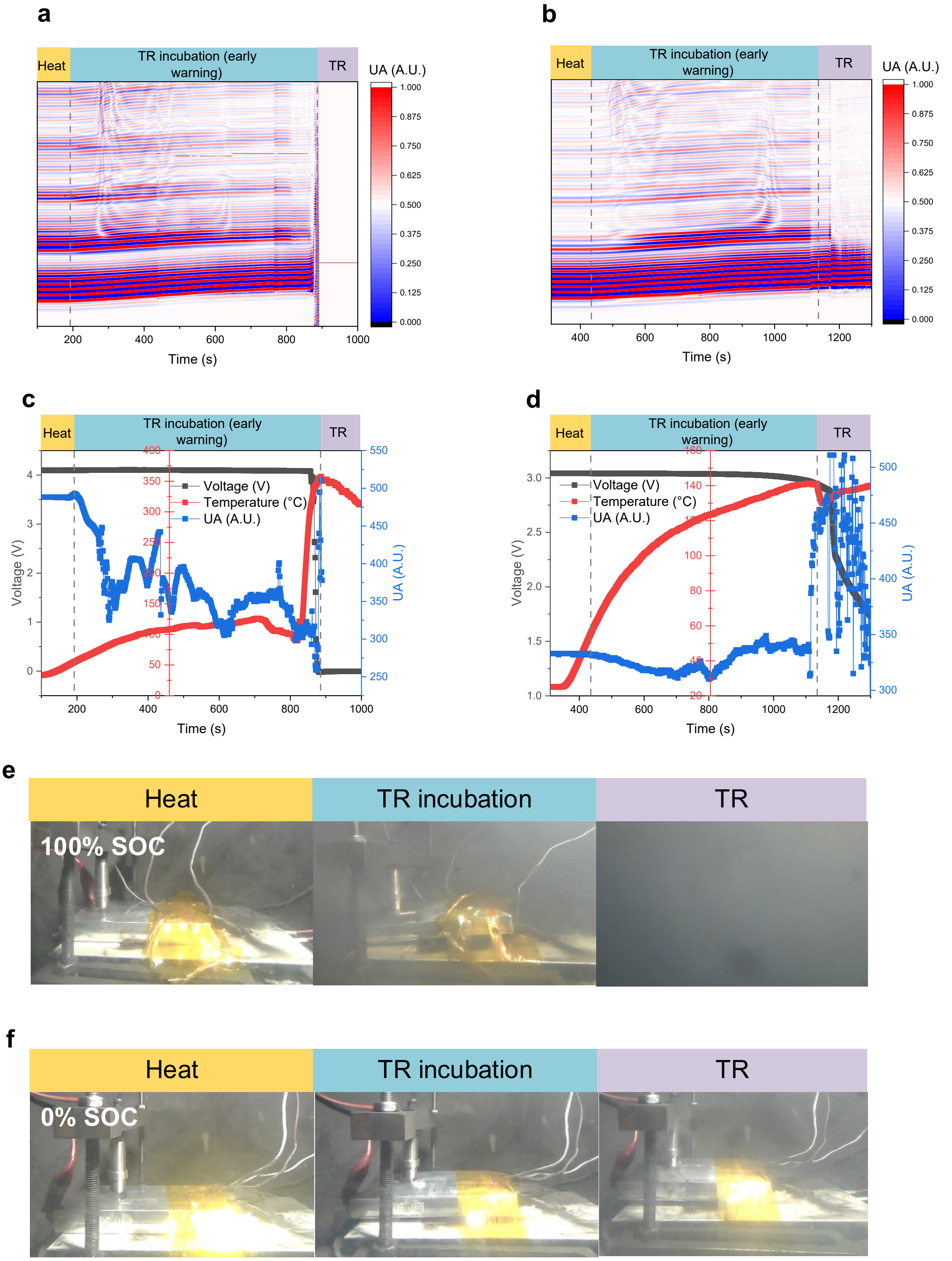

Fig. S9. Ultrasonic early warning of TR for LMO prismatic cells. Heatmaps of ultrasonic waves for (**a**) 100% SOC and (**b**) 0% SOC cells. The change of UA, temperature and voltage during the TR of (**c**) 100% SOC and (**d**) 0% SOC cells. Photographs of thermal abuse process of (**e**) 100% SOC and (**f**) 0% SOC prismatic cells.

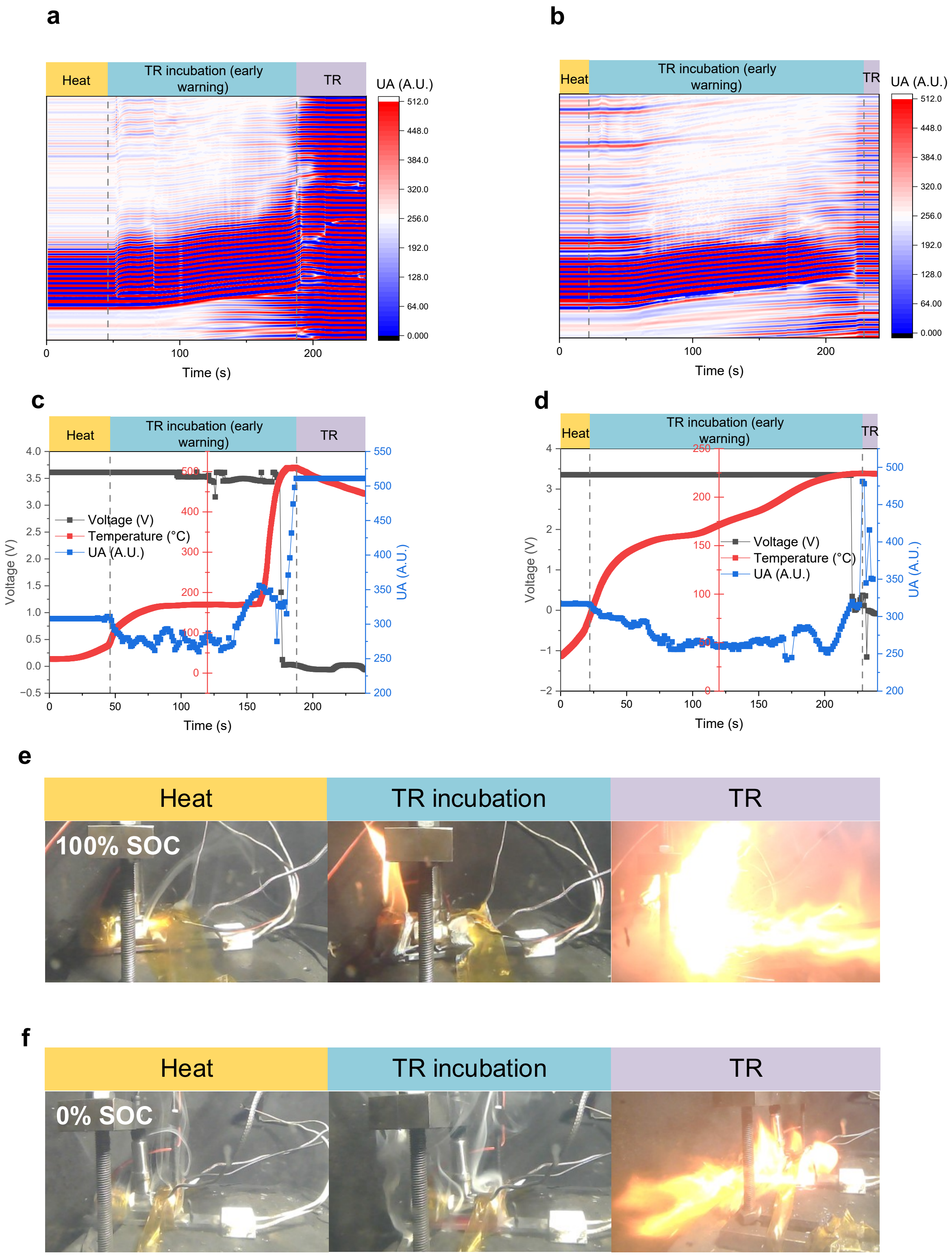

Fig. S10. Ultrasonic early warning of TR for LMO cylindrical cells. Heatmaps of ultrasonic waves for (**a**) 100% SOC and (**b**) 0% SOC cells. The change of UA, temperature and voltage during the TR of (**c**) 100% SOC and (**d**) 0% SOC cells. Photographs of thermal abuse process of (**e**) 100% SOC and (**f**) 0% SOC cylindrical cells.

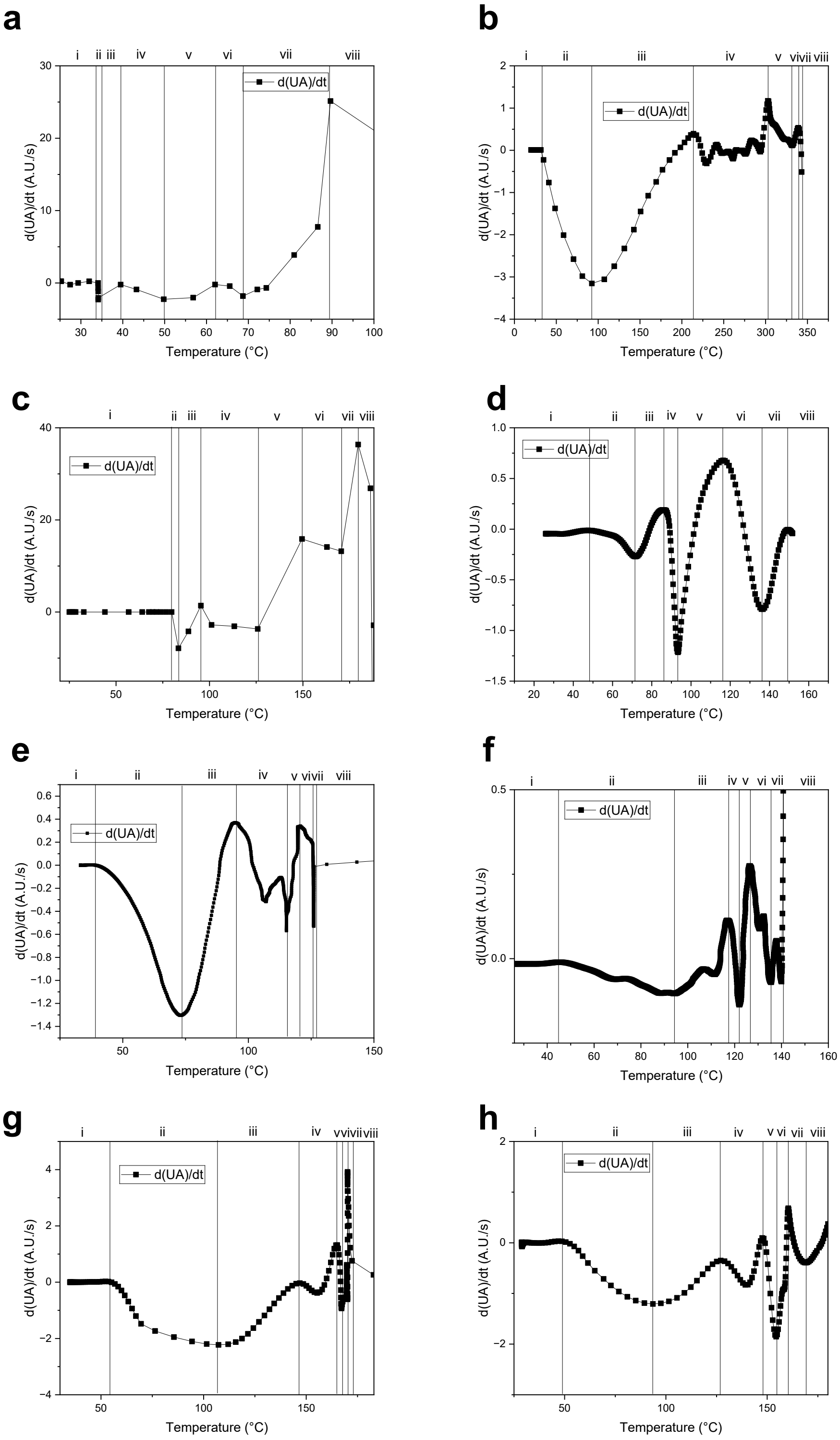

Fig. S11. Ultrasonic Interpretation of Failure Mechanism for varying chemistries and formats cells. d(UA)/dt versus temperature of (**a**) 100% SOC and (**b**) 0% SOC NCM pouch cells. d(UA)/dt versus temperature of (**c**) 100% SOC and (**d**) 0% SOC LFP pouch cells. d(UA)/dt versus temperature of (**e**) 100% SOC and (**f**) 0% SOC LMO prismatic cells. d(UA)/dt versus temperature of (**g**) 100% SOC and (**h**) 0% SOC NCM cylindrical cells.
The stages are the same as the LMO pouch cell in manuscript.

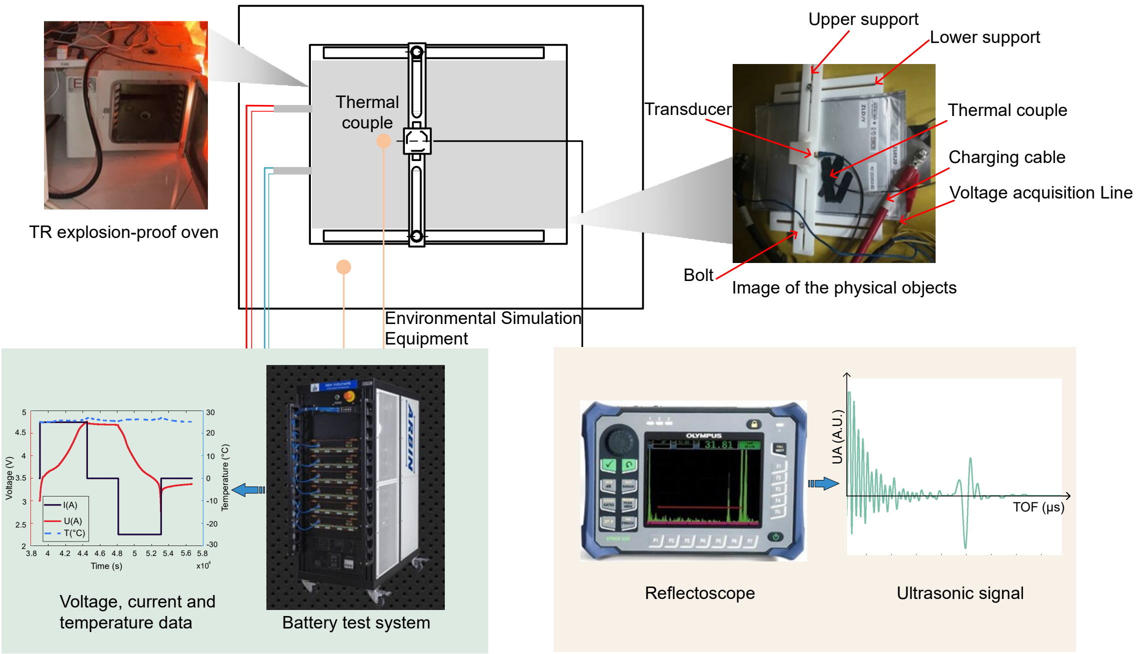

Fig. S12. Ultrasonic testing platform.

Supplemental Tables

Table S1. Correlation coefficients of the ΔTOF_{t}-temperature relationships.

Cell type	SOC (%)	Tempertaure (°C)				
		5	15	25	35	45
NCM pouch cell	0	0.9998	0.9999	0.9999	0.9997	0.9998
	25	0.9997	0.9998	0.9998	0.9998	0.9998
	50	0.9999	0.9997	0.9997	0.9995	0.9998
	75	0.9996	0.9999	0.9998	0.9997	0.9998
	100	0.9995	0.9998	0.9999	0.9996	0.9998
LFP pouch cell	0	0.9995	0.9999	0.9999	0.9998	0.9999
	25	0.9997	0.9999	0.9998	0.9998	0.9999
	50	0.9998	0.9999	0.9999	0.9996	0.9999
	75	0.9997	0.9998	0.9999	0.9999	0.9998
	100	0.9996	0.9999	0.9999	0.9998	0.9997
LMO prismatic cell	0	0.9997	0.9997	0.9996	0.9996	0.9996
	25	0.9997	0.9996	0.9995	0.9996	0.9996
	50	0.9996	0.9995	0.9998	0.9997	0.9995
	75	0.9995	0.9995	0.9995	0.9999	0.9999
	100	0.9998	0.9995	0.9999	0.9998	0.9999
NCM cylindrical cell	0	0.9998	0.9996	0.9997	0.999	0.999
	25	0.9998	0.9998	0.9998	0.9997	0.9999
	50	0.9999	0.9997	0.9999	0.9997	0.9998
	75	0.9999	0.9999	0.9999	0.9997	0.9999
	100	0.9998	0.9996	0.9998	0.9999	0.9999

Table S2. Experimental results of ultrasonic estimation of specific heat capacity.

Number	Experiments	Methods
1	SOC=50%	(1) Place the battery in an environmental simulation device at an ambient temperature of 25°C and let it stand for 30 minutes; (2) Discharge at 1C CC to cut-off voltage and let stand for 1 hour; (3) Charge at 1C CC for 30 minutes and let stand for 4 hours.
2	5°C specific heat capacity test	(1) Set the ambient temperature to 5 °C and let it stand for 2 hours. (2) Discharge at 2C CC for 3 seconds; (3) Charge at 2C CC for 3 seconds; (4) Repeat steps (2) and (3) 1200 times; (5) Let stand for 2 hours.
3	Specific heat capacity test at 15°C, 25°C, 35°C and 45°C	(1) Set the ambient temperature to 15 °C for 2 hours; (2) Discharge CC at 3C power for 3 seconds; (3) Charge at 3C CC for 3 seconds; (4) Repeat steps (2) and (3) 1200 times; (5) Stand for 2 hours; (6) Set the ambient temperature to 25 °C, 35 °C and 45 °C successively, and let it stand at each temperature point for 2 hours and repeat steps (2-5).

Table S3. Ultrasonic estimation results of thermal characteristics with LMO pouch cell.

T (°C)	*k*	Ultrasonic C_p (J/(kg·K))	ARC C_p (J/(kg·K))	MAPE (%)
5	118.363	1275.4	1250.02	1.99
15	121.95	1260.25	1298.81	3.06
25	126.82	1336.8	1377.97	3.08
35	142.96	1379.21	1421.97	3.10
45	149.57	1428.57	1487.99	4.16

Table S4. Ultrasonic estimation results of thermal characteristics with NCM pouch cell and LFP pouch cell.

Cell chemistry	T (°C)	k	Ultrasonic C_p (J/(kg·K))	ARC C_p (J/(kg·K))	MAPE (%)
NCM	5	0.0425	578.45	574.35	0.71
	15	0.0436	676.77	686.66	1.44
	25	0.0446	760.23	737.82	3.06
	35	0.0458	743.06	766.36	3.03
	45	0.0469	817.28	784.79	4.14
LFP	5	0.0231	703.49	675.56	4.13
	15	0.0251	802.25	798.08	0.52
	25	0.0217	821.40	852.91	3.70
	35	0.0260	845.17	881.81	4.15
	45	0.0254	861.12	898.33	4.14

Table S5. Ultrasonic estimation results of thermal characteristics with LMO prismatic cell and NCM cylindrical cell.

Cell format	T (°C)	k	Ultrasonic C_p (J/(kg·K))	ARC C_p (J/(kg·K))	MAPE (%)
Prismatic cell	5	0.0483	550.72	528.97	4.11
	15	0.0501	658.14	640.79	2.71
	25	0.0519	713.30	695.20	2.60
	35	0.0537	754.12	724.56	4.08
	45	0.0545	773.92	743.22	4.13
Cylindrical cell	5	0.0242	623.90	644.90	3.26
	15	0.0247	797.90	818.89	2.56
	25	0.0253	938.76	911.35	3.00
	35	0.0259	941.62	975.74	3.50
	45	0.0272	988.22	1025.66	3.65

References

1. Z. Deng, Z. Huang, Y. Shen, Y. Huang, H. Ding, A. Luscombe, M. Johnson, J. E. Harlow, R. Gauthier and J. R. Dahn, *Joule*, 2020, **4**, 2017-2029.
2. B. K. Purushothaman, P. W. Morrison and U. Landau, *J. Electrochem. Soc.*, 2005, **152**, J33.
3. Y. Inui, Y. Kobayashi, Y. Watanabe, Y. Watase and Y. Kitamura, *Energy Convers. Manag.*, 2007, **48**, 2103-2109.
4. S. Mirza, C. H. Amon and S. Chandra, presented in part at the 2023 22nd IEEE Intersociety Conference on Thermal and Thermomechanical Phenomena in Electronic Systems (ITherm), 2023, 2023.